J. Phys.: Condens. Matter **23** (2011) 015003 (14pp) doi:10.1088/0953-8984/23/1/015003

Rubber friction and tire dynamics

B N J Persson[1]

IFF, FZ-Jülich, D-52428 Jülich, Germany

Received 15 July 2010, in final form 20 October 2010
Published 26 November 2010
Online at stacks.iop.org/JPhysCM/23/015003

Abstract

We propose a simple rubber friction law, which can be used, for example, in models of tire (and vehicle) dynamics. The friction law is tested by comparing numerical results to the full rubber friction theory (Persson 2006 *J. Phys.: Condens. Matter* **18** 7789). Good agreement is found between the two theories.

We describe a two-dimensional (2D) tire model which combines the rubber friction model with a simple mass–spring description of the tire body. The tire model is very flexible and can be used to accurately calculate μ-slip curves (and the self-aligning torque) for braking and cornering or combined motion (e.g. braking during cornering). We present numerical results which illustrate the theory. Simulations of anti-blocking system (ABS) braking are performed using two simple control algorithms.

(Some figures in this article are in colour only in the electronic version)

1. Introduction

Rubber friction is a topic of huge practical importance, e.g. for tires, rubber seals, wiper blades, conveyor belts and syringes [1–18]. In most theoretical studies rubber friction is described using very simple phenomenological models, e.g. the Coulomb friction law with a friction coefficient which may depend on the local sliding velocity. However, as we have shown earlier [6], rubber friction depends on the history of the sliding motion (memory effects), which we have found to be crucial for an accurate description of rubber friction. For rubber sliding on a hard rough substrate, the history dependence of the friction is mainly due to frictional heating in the rubber–substrate contact regions. Many experimental observations, such as an apparent dependence of the rubber friction on the normal stress, can be attributed to the influence of frictional heating on the rubber friction.

A huge number of papers have been published related to tire dynamics, in particular in the context of anti-blocking system (ABS) braking models. The 'heart' in tire dynamics is the road–rubber tire friction. Thus, unless this friction is accurately described, no tire model, independent of how detailed the description of the tire body may be, will provide an accurate picture of tire dynamics. However, most treatments account for the road–tire friction in a very approximate way. Thus, many 'advanced' finite element studies for tire dynamics account for the friction only via a static and a kinetic rubber friction coefficient. In other studies the dynamics of the whole tire is described using interpolation formulae, e.g. the 'magic formula' [4], but this approach requires a very large set of measured tire properties (which are expensive and time-consuming to obtain), and cannot describe the influence of history (or memory) effects on tire dynamics.

In this paper we first propose a very simple rubber friction law (with memory effects) which gives nearly identical results to the full model developed in [6]. We also develop a 2D tire model which combines the rubber–road friction theory (which accounts for the flash temperature) with a simple two-dimensional (2D) description of the tire body. We believe that the most important aspect of the tire body is its distributed mass and elasticity, and this is fully accounted for in our model. One advantage of the 2D model over a full 3D model is that one can easily impose any footprint pressure distribution one likes (e.g. measured pressure distributions), while in a 3D model the pressure distribution is fixed by the model itself. This allows a detailed study on how sensitively the tire dynamics depend on the nature of the footprint pressure distribution. The tire model is illustrated by calculating μ-slip curves and with simulations of ABS braking using two different control algorithms.

2. Rubber friction

Rubber friction depends on the history of the sliding motion. This is mainly due to the flash temperature: the temperature in the rubber–road asperity contact regions at time t depends on the sliding history for all earlier times $t' < t$. This memory effect is crucial for an accurate description of rubber friction. We illustrate this effect in figure 1 for a rubber tread block

[1] www.MultiscaleConsulting.com.

 © 2011 IOP Publishing Ltd Printed in the UK & the USA

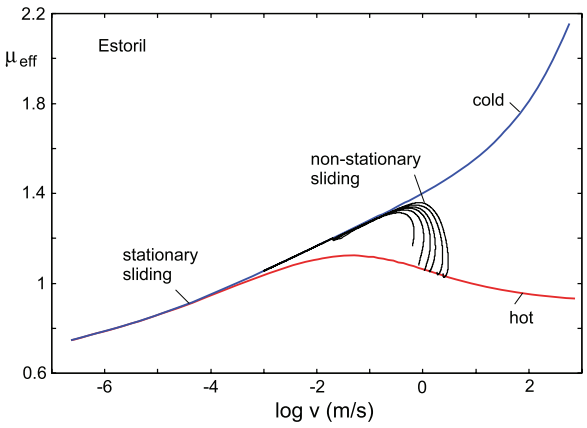

Figure 1. Red and blue lines: the kinetic friction coefficient (stationary sliding) as a function of the logarithm (with 10 as basis) of the sliding velocity. The blue line denoted 'cold' is without the flash temperature while the red line denoted 'hot' is with the flash temperature. Black curves: the effective friction experienced by a tread block as it goes through the footprint. For a car velocity 27 m s^{-1} and for several slip values 0.005, 0.0075, 0.01, 0.03, 0.05, 0.07 and 0.09. Note that the friction experienced by the tread block first follows the 'cold' rubber branch of the steady state kinetic friction coefficient and then, when the block has slip a distance of the order of the diameter of the macroasperity contact region, it follows the 'hot' rubber branch.

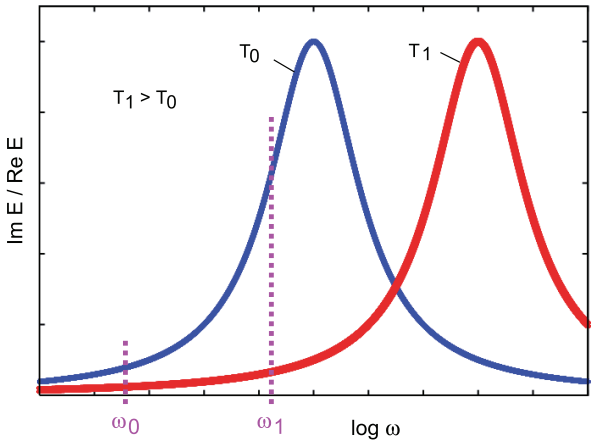

Figure 2. When the temperature increases the $\tan\delta = \mathrm{Im}\,E/\mathrm{Re}\,E$ spectra shift to higher frequencies, which result in a decrease in the rubber friction. We assume the road asperities give rise to pulsating frequencies in the range ω_0 and ω_1.

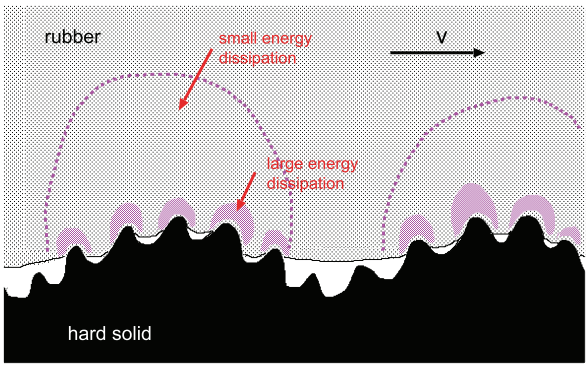

Figure 3. The dissipated energy per unit volume is highest in the smallest asperity contact regions.

sliding on an asphalt road surface. We show the (calculated) kinetic friction coefficient for stationary sliding without (blue curve) and including (red curve) the flash temperature as a function of the velocity v of the bottom surface of the rubber block. The black curves show the effective friction during non-stationary sliding experienced by a rubber tread block during braking at various slips (slip values from 0.005 to 0.09). Note that, because some finite sliding distance is necessary in order to fully develop the flash temperature, the friction acting on the tread block initially follows the blue curve corresponding to 'cold rubber' (i.e. negligible flash temperature). Thus, it is not possible to accurately describe rubber friction with just a static and a kinetic friction coefficient (as is often done even in advanced tire dynamics computer simulation codes) or even with a function $\mu(v)$ which depends on the instantaneous sliding velocity $v(t)$. Instead, the friction depends on $v(t')$ for all times $t' \leqslant t$.

As a background to what follows, we first review the rubber friction theory (see [5, 6] for details). It is assumed that all energy dissipation arises from the viscoelastic deformations of the rubber surface by the road asperities. An asperity contact region with the diameter d gives rise to time-dependent (pulsating) deformations of the rubber which is characterized by the frequency $\omega = v/d$, where v is the sliding velocity. The viscoelastic deformation (and most of the energy dissipation) extends into the rubber by the typical distance d. So most of the energy dissipation occurs in a volume element of order d^3. In order to have a large asperity-induced contribution to the friction the frequency ω should be close to the maximum of the $\tan\delta = \mathrm{Im}\,E(\omega)/\mathrm{Re}\,E(\omega)$ curve. Here $E(\omega)$ is the viscoelastic modulus of the rubber. In reality there will be a wide distribution of asperity contact sizes, so there will be a wide range of perturbing frequencies, say from ω_0 to ω_1, see figure 2. A large friction requires that $\tan\delta$ is as large as possible for all these perturbing frequencies.

The temperature dependence of the viscoelastic modulus of rubber-like materials is usually very strong, and an increase in the temperature by 10 °C may shift the $\tan\delta$ curve to higher frequencies by one frequency decade. This will usually reduce the rubber friction, see figure 2.

Real surfaces have a wide distribution of asperity sizes. The best picture of a rough surface is to think about it as large asperities on top of which occur smaller asperities on top of which occur even smaller asperities, and so on. This is illustrated in figure 3 for a case where roughness occurs on two length scales. To get the total energy dissipation during sliding on a real surface one needs to sum up the contribution from asperity-induced deformation of the rubber on all (relevant) length scales. It is important to note that all length scales are *a priori* equally important [5].

Temperature has a crucial influence on rubber friction. The viscoelastic energy dissipation, which is the origin of the rubber friction in my model, results in local heating of the rubber in exactly the region where the energy dissipation occur. This results in a temperature increase, which becomes

larger as we observe smaller and smaller asperity contact regions. This local (in time and space) temperature increase, resulting from the local viscoelastic energy dissipation, is referred to as the flash temperature. The flash temperature has an extremely important influence on the rubber friction. This is illustrated in figure 1, where we show the (calculated) steady state kinetic friction coefficient when a block of tread rubber is sliding on an asphalt road surface. The upper curve is the result without accounting for the flash temperature, i.e. the temperature is assumed to be equal to the background temperature T_0 everywhere. The lower curve is the result including the flash temperature. Note that for sliding velocities $v > 0.001$ m s^{-1} the flash temperature results in a lowering of the sliding friction. For velocities $v < 0.001$ m s^{-1} the produced heat has enough time to diffuse away from the asperity contact regions, and the flash temperature effect is negligible.

In the rubber friction theory the concept of the macroasperity contact region is of crucial importance. Let us study the footprint contact region between a tire and a road surface at different magnification ζ. At low magnification the road surface appears smooth and the contact between the tire and the road appears to be complete within the footprint area as in figure 4(a). However, when we increase the magnification ζ we start to observe non-contact regions as in figure 4(b). At high enough magnification we observe isolated contact regions as in figure 4(c), which, when the magnification increases even further, break up into even smaller contact regions as in figure 4(d). We denote the contact regions observed in figure 4(c) as the macroasperity contact regions (with average diameter D), and we denote the corresponding magnification by ζ_c. Formally, we defined ζ_c to be the magnification where the second derivative of $\log P(\zeta)$ with respect to $\log \zeta$ has its first maximum with increasing ζ (see [6, 20]). If the nominal pressure in the tire–road contact region is small enough, the macroasperity contact regions will be well separated, but the separation between the microasperity contact regions within the macroasperity contact regions is, in general, very small. When calculating the flash temperature effect we have therefore smeared out the heat produced by the microasperity contact regions uniformly within the macroasperity contact regions. Typically for road surfaces $D \approx 0.1$–1 cm and the fraction of the tread block surface occupied by the macroasperity contact regions is typically between 10% and 30%.

In the friction theory developed in [6] only the surface roughness with wavevectors $q < q_1$ is assumed to contribute to the friction. For clean road surfaces we determine the cutoff wavevector q_1 by a yield condition: we assume that the local stress and temperature in the asperity contact regions on the length scale $1/q_1$ are so high that the rubber bonds break, resulting in a thin modified (dead) layer of rubber at the surface region of thickness $\approx 1/q_1$. (In the alternative theory of Kluppel and Heinrich [8] another mechanism for obtaining q_1 was proposed.) From this follows the following observations:

(a) The rubber friction on clean road surfaces after run-in is rather insensitive to the road surface. This has been observed in several series of experimental studies (not shown), and is in accordance with the present theory. This can be understood as follows. The cutoff q_1 on surfaces with smoother, less sharp roughness or surfaces where the roughness occurs at shorter length scales will be larger (i.e. the cutoff wavelength $\lambda_1 = 2\pi/q_1$ smaller) than for road surfaces with larger roughness in such a way that the stress and temperature increase in the asperity contact regions which can be observed at the resolution λ_1 (or magnification $\zeta = q_1/q_0$) are roughly the same on all surfaces. This implies that a larger range of roughness will contribute to the rubber friction on 'smoother' surfaces as compared to more rough surfaces. As a consequence, the friction (after run-in) may vary very little between different (clean) road surfaces.

(b) On contaminated road surfaces, the cutoff q_1 may be determined by the nature of the contamination. In this case, if the cutoff is fixed (e.g. determined by, say, the size of contamination particles) one may expect much larger variation in the friction coefficient between different road surfaces, and also a larger variation between tires with different types of tread rubber.

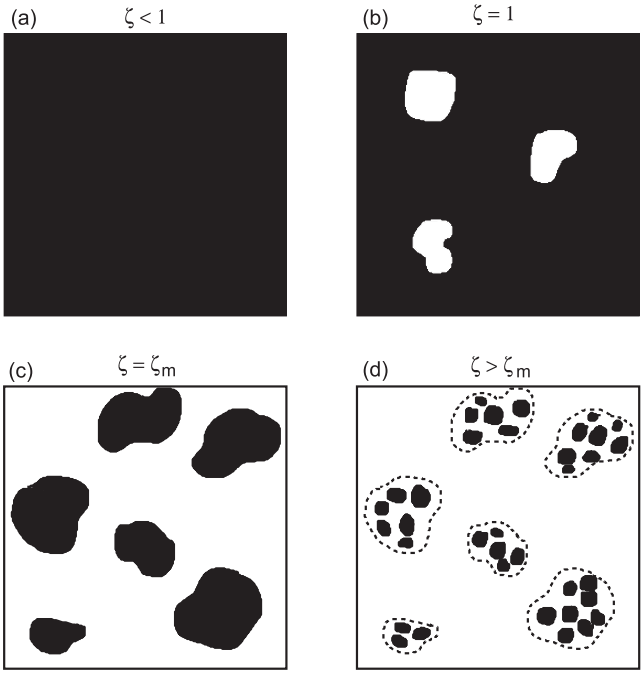

Figure 4. The contact region between a tire and a road surface. At low magnification $\zeta < 1$ it appears that the tire is in complete contact with the road but, as the magnification increases, the contact area continuously decreases as indicated in the figure.

The mechanism we have proposed for the determination of q_1, namely the formation of a thin modified (dead) layer at the rubber surface as a result of the high stresses and temperatures the tread rubber surface is exposed to during slip, is closely related to rubber wear. Rubber wear occurs during slip, and the track gets contaminated by small wear particles which may have some influence on the sliding friction. We have observed rubber wear in indoor rubber friction experiments, and it is also well known to occur when a car brakes on a road (leaving

dark (black) regions of rubber particles on the road surface). However, we do not expect the wear particles to have a large influence on the observed friction since most of them are of similar size as the cutoff distance determined by the strength of the rubber, and during modest slip they cover only a small part of the road surface. This is supported by our lab experiments where we observe a negligible change in the rubber friction force when the same rubber tread element (or rubber block) slides a second time on the same (not cleaned) road track, or even on a (much smoother) grinded steel surface [19].

The cutoff length $1/q_1$ depends on the rubber compound used and on the nature of the road surface (so changing the road surface requires some short run-in in order for a new thin modified surface layer to form on the tread block (corresponding to a new cutoff length)). In this paper we have used two different tread compounds for which the cutoff length was optimized for the Estoril race track using the procedure described in [6].

Based on the picture presented above, in [6] we have derived a set of equations describing the friction acting on a rubber block squeezed with a stress σ_0 against a hard randomly rough surface. Here we summarize the basic equations. The frictional stress $\sigma_f = \mu(t)\sigma_0$ depends on the history of the sliding motion (velocity $v(t) = \dot{x}(t)$) via the following set of equations:

$$\mu(t) \approx \tfrac{1}{2}\int_{q_0}^{q_1} \mathrm{d}q\, q^3 C(q) P(q,t) \times \int_0^{2\pi} \mathrm{d}\phi \cos\phi\, \mathrm{Im}\, \frac{E(qv(t)\cos\phi, T_q(t))}{(1-\nu^2)\sigma_0}.$$

In this equation enters the flash temperature at time t:

$$T_q(t) = T_0 + \int_0^t \mathrm{d}t'\, \Gamma(t,t') \int_0^\infty \mathrm{d}q'\, f(q',t') \times \frac{1}{\pi}\int_0^\infty \mathrm{d}k\, \frac{4q^2}{k^2+4q^2}\frac{4q'}{k^2+4q'^2} \mathrm{e}^{-Dk^2(t-t')}$$

where $\Gamma(t,t') = h(w(t,t'))$ with

$$h(w) = 1 - \frac{2}{\pi} w\left(1-w^2\right)^{1/2} - \frac{2}{\pi}\arcsin w,$$

for $w < 1$ and $h(w) = 0$ for $w > 1$, and where $w(t,t') = [x(t) - x(t')]/2R$ depends on the history of the sliding motion. The function

$$f(q,t) = \frac{v(t)}{\rho C_v} q^4 C(q) \frac{P(q,t)}{P(q_\mathrm{m},t)} \times \int \mathrm{d}\phi\, \cos\phi\, \mathrm{Im}\, \frac{E(qv(t)\cos\phi, T_q(t))}{1-\nu^2},$$

where $v = \dot{x}(t)$ depends on time. The function $P(q,t)$ (which also depends on time) is given by

$$P(q,t) = \frac{2}{\pi}\int_0^\infty \mathrm{d}x\, \frac{\sin x}{x} \exp[-x^2 G(q,t)] = \mathrm{erf}\left(\frac{1}{2\sqrt{G}}\right)$$

where

$$G(q,t) = \frac{1}{8}\int_{q_0}^{q} \mathrm{d}q\, q^3 C(q) \int_0^{2\pi} \mathrm{d}\phi \left|\frac{E(qv(t)\cos\phi, T_q(t))}{(1-\nu^2)\sigma_0}\right|^2.$$

We refer to this theory as the 'full theory'.

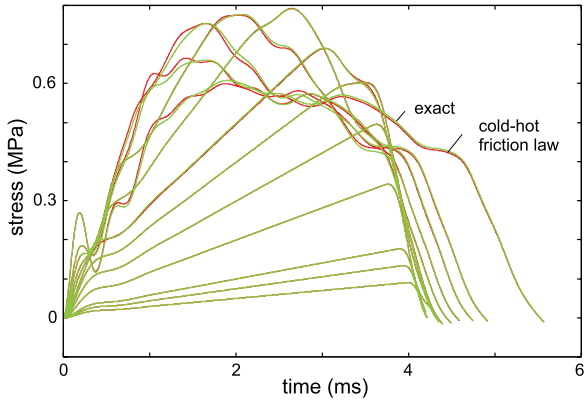

Figure 5. The frictional shear stress acting on a tread block as a function of time for many slip values: 0.005, 0.0075, 0.01, 0.03, 0.05, 0.07, 0.09, 0.12, 0.15 and 0.25. For the car velocity 27 m s^{-1} and tire background temperature $T_0 = 60\,^\circ$C. For the 1D tire model using the full friction model (green curves) and the cold–hot friction law (1) (red curves). For a passenger car tread compound.

3. Phenomenological rubber friction law

In tire applications, for slip of the order of 5–10% and typical footprint length of the order of 10 cm, the slip distance of a tread rubber block in the footprint will be of the order of 1 cm, which typically is of the order of the diameters D of the macroasperity contact regions. As discussed above, as long as the slip distance $r(t)$ is small compared to D one follows the cold-rubber branch of the steady state relation $\mu(v)$ so that $\mu(t) \approx \mu_\mathrm{cold}(v(t))$ for the slip distance $r(t) \ll D$. When the tread block moves towards the end of the footprint the slip distance $r(t)$ may be of the order of (or larger than) D, and the friction will follow the hot branch of the $\mu(v)$ relation, i.e. $\mu(t) \approx \mu_\mathrm{hot}(v(t))$ for $r(t) > D$. We have found that the following (history-dependent) friction law gives nearly the same result as the full theory presented above and in [6]:

$$\mu(t) = \mu_\mathrm{cold}(v(t), T_0)\mathrm{e}^{-r(t)/0} + \mu_\mathrm{hot}(v(t), T_0)[1 - \mathrm{e}^{-r(t)/r_0}] \tag{1}$$

where $v(t)$ is the instantaneous sliding velocity, $r(t)$ the sliding distance and $r_0 \approx 0.2D$. We will refer to (1) as the cold–hot friction law. The length D depends on the rubber compound and the road surface but is typically in the range $D \approx 0.1$–1 cm. Using the full friction theory one can easily calculate the functions $\mu_\mathrm{cold}(v, T_0)$ and $\mu_\mathrm{hot}(v, T_0)$ and the length D.

To demonstrate the accuracy of the cold–hot rubber friction law (1), let us study the dynamics of one tread block as it passes through the tire–road footprint. In figure 5 we show the frictional shear stress acting on a tread block as a function of time for many slip values: 0.005, 0.0075, 0.01, 0.03, 0.05, 0.07, 0.09, 0.12, 0.15 and 0.25. Note that the cold–hot friction law (1) (red curves) gives nearly the same result as for the full friction model (green curves). In figure 6 we show the μ-slip curve. Again the cold–hot friction law (1) (red curve) gives nearly the same result as the full friction model (green curve).

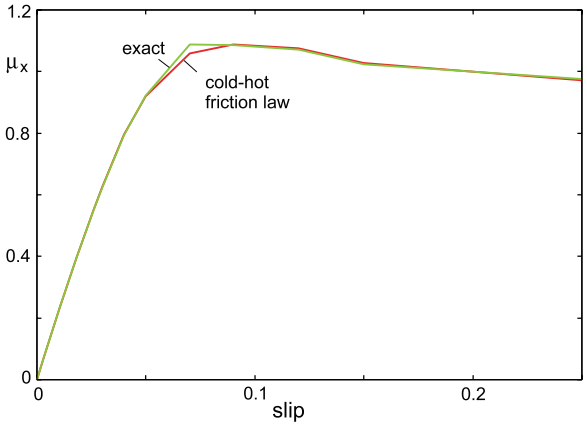

Figure 6. The μ-slip curve for the 1D tire model using the full friction model (green curve) and the cold–hot friction law (1) (red curve). For a passenger car tread compound.

4. Tire dynamics

All the calculations presented in this section have been obtained using the 2D tire model described below, with the tire body optimized using experimental data for a passenger car tire. The viscoelastic springs associated with this tire body are kept fixed in all the calculations. Thus the model calculations do not take into account the changes in the tire body viscoelastic properties due to variations in the tire (background) temperature or variations in the tire inflation pressure (which affect the tension in the tire walls). In principle both effects can be relatively simply accounted for in the model, but have not been included so far. The calculations presented below are obtained using the measured viscoelastic modulus of two tire tread compounds, and for the Estoril race track.

We emphasize that the present model is not a 'stationary tire model', but the model describes arbitrarily complex tire dynamics, e.g. combined (time-dependent) variation in the longitudinal slip, the cornering angle and the camber angle, while the (forward or rolling) velocity may depend on time in any arbitrary way. We solve numerically the full (time-dependent) set of equations of motion without any limitation. In fact, even 'stationary tire motion' involves non-steady tread block motion. Thus, at small slip a tread block when entering the footprint is first (nearly) pinned to the substrate, and only close to the exit of the footprint will it undergo fast slip. Furthermore, after leaving the footprint the tread block may perform damped high-frequency vibrations for a short time (resulting in high-frequency noise); this is all accurately described by the tire model although not discussed in the present paper.

In our model the tire is discretized into blocks as described below. To each tire body element in the tread area is 'connected' a tread block which in turn is discretized in the vertical direction into many (typically 10) thin block elements (describing vertical slices of the tread block), which are coupled to each other using viscoelastic springs (corresponding to the measured viscoelastic modulus of the tread rubber) as described in detail in [6]. This model also allows for a gradient in the tread rubber properties, as is typical in real applications (where a stiffer, less hysteretic, rubber is often used in the upper part of the tread block in order to reduce (stabilize) the deformations of the tread block when exposed to large stresses, and in order to reduce the rolling resistance). The parallel (frictional) stress which acts on a tread block is the product of the normal stress times the friction coefficient, which depends on the history of the sliding motion of the tread block element, as described by the theory of [6], or by the simplified friction law given by (1). Thus the present theory includes the memory effects of the friction force resulting from the non-uniform (in time) slip motion of the tread blocks.

The present study only accounts for frictional heating via the flash temperature effect. In reality the background temperature T_0 may also change with time, e.g. during ABS braking, or during measurement of the μ-slip curve. (It is well known in indoor measurements of tire μ-slip curves that the increase in T_0 with increasing time may result in large 'hysteresis' if the slip is first increased from zero to unity, and then reduced back to zero; see [3].) We have not included this effect so far, but it can relatively easily be included in the present theory. There is also another temperature effect coming from the overlap of hot spots from different asperity contact regions which is not included in this study (see below).

The flash temperature depends on both the slip velocity and the slip distance. The amount of dissipated energy (which is the product of friction force and slip distance) goes to zero as the slip distance goes to zero so negligible frictional heating (and negligible temperature increase) of the rubber will occur when the slip distance is very small. On the other hand, when the slip distance becomes larger than the diameter D of the macroasperity contact regions then there is no longer any overlap between the present (say, at time t) contact region and the original (say, at time $t = 0$) macroasperity contact region, and at this point the flash temperature has been fully developed. This picture neglects the fact that after long enough slip a given macroasperity contact region may overlap with the 'hot rubber track' emerging from another asperity contact region in front of it (note: this hot rubber track will widen in time due to heat diffusion, and finally (for long enough time) contribute to the background temperature $T_0(t)$). This effect is also included as an option in our computer code, but was not activated in the present study as we are still working on how to best describe this effect. However, this effect is not important for slip up to (and slightly beyond) the point where the μ-slip curve has its maximum, which is the most important region of slip for practical applications (e.g. ABS braking), but will give rise to a decrease in the friction for large slip.

We use a 2D description of the tire body as indicated in figure 7. We introduce a coordinate system with the y axis in the transverse direction and the x axis along the longitudinal (rolling) direction. We consider the tire–road system in a reference frame where the road is stationary. The car velocity $v_c(t)$, the rolling velocity $v_R(t)$ and the cornering angle $\theta(t)$ determine the transverse $v_y(t)$ and longitudinal $v_x(t)$ slip velocities:

$$v_y = v_c \sin\theta \qquad v_x = v_c \cos\theta - v_R.$$

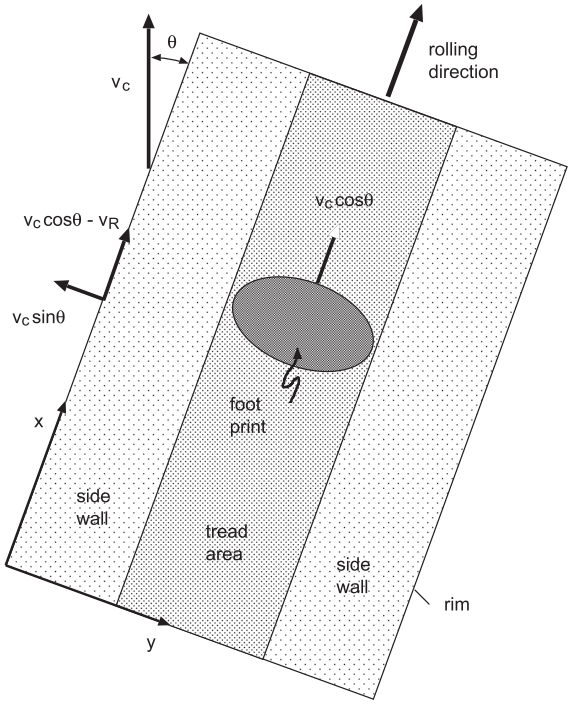

Figure 7. 2D model of a tire. The car velocity $\mathbf{v}_c$ points in another direction than the rolling direction, giving a non-zero cornering angle θ.

The longitudinal slip $s(t)$ is defined by

$$s = \frac{v_x}{v_c \cos\theta} = \frac{v_c \cos\theta - v_R}{v_c \cos\theta}.$$

When the cornering angle $\theta = 0$ this equation reduces to

$$s = \frac{v_c - v_R}{v_c}.$$

For non-stationary tire dynamics, the slip $s(t)$ and the cornering angle $\theta(t)$ will depend on time t. Note that v_x and v_y are also the velocities of the tire rim, and that the footprint moves (in the rolling direction) with the velocity $v_c \cos\theta$ relative to the road, and with the rolling velocity $v_c \cos\theta - v_x = v_R$ relative to the rim.

We describe the tire body as a set of mass points connected with viscoelastic springs (elasticity k and viscous damping γ). The springs have both elongation and bending elasticity, denoted by k and k', respectively, and the corresponding viscous damping coefficients γ and γ'. We assume N_x and N_y tire body blocks along the x and y directions and let $\mathbf{x}_{ij} = (x_{ij}, y_{ij})$ denote the displacement vector of the tire body block (i, j) $(i = 1, \ldots, N_x, j = 1, \ldots, N_y)$. Since the tire is a torus-shaped object we must assume periodic boundary conditions in the x direction so that $x_{N_x+1,j} = x_{1,j}$ and $y_{N_x+1,j} = y_{1,j}$.

We have the following boundary conditions. For $i = 0, \ldots, N_x + 1$:

$$\dot{y}_{i0} = v_y, \qquad \dot{x}_{i0} = v_x$$

$$\dot{y}_{i,N_y+1} = v_y, \qquad \dot{x}_{i,N_y+1} = v_x.$$

For stationary tire motion these equations reduce to

$$y_{i0} = v_y t, \qquad x_{i0} = v_x t$$

$$y_{i,N_y+1} = v_y t, \qquad x_{i,N_y+1} = v_x t.$$

For $j = 1, \ldots, N_y$ we have the periodic boundary conditions:

$$y_{N_x+1,j} = y_{1j}, \qquad x_{N_x+1,j} = x_{1j}$$

$$y_{0j} = y_{N_x,j}, \qquad x_{0j} = x_{N_x,j}.$$

If the mass of tire body element (i, j) is denoted by m_j, we get for $i = 1, \ldots, N_x$, $j = 1, \ldots, N_y$:

$$\begin{aligned} m_j \ddot{y}_{ij} &= F_{yij} + k_{yj}(y_{i,j-1,} - y_{ij}) + k_{yj+1}(y_{i,j+1} - y_{ij}) \\ &\quad + \gamma_{yj}(\dot{y}_{i,j-1} - \dot{y}_{ij}) + \gamma_{yj+1}(\dot{y}_{i,j+1} - \dot{y}_{ij}) \\ &\quad + k'_{xj}(y_{i+1,j} + y_{i-1,j} - 2y_{ij}) \\ &\quad + \gamma'_{xj}(\dot{y}_{i+1,j} + \dot{y}_{i-1,j} - 2\dot{y}_{ij}) \\ m_j \ddot{x}_{ij} &= F_{xij} + k_{xj}(x_{i-1,j} - x_{ij}) + k_{xj}(x_{i+1,j} - x_{ij}) \\ &\quad + \gamma_{xj}(\dot{x}_{i-1,j} - \dot{x}_{ij}) + \gamma_{xj}(\dot{x}_{i+1,j} - \dot{x}_{ij}) \\ &\quad + k'_{yj}(x_{i,j-1} - x_{ij}) + k'_{yj+1}(x_{i,j+1} - x_{ij}) \\ &\quad + \gamma'_{yj}(\dot{x}_{i,j-1} - \dot{x}_{ij}) + \gamma'_{yj+1}(\dot{x}_{i,j+1} - \dot{x}_{ij}). \end{aligned}$$

In the equations above, F_{xij} and F_{yij} are the force components (in the x and y directions, respectively) acting on the tire body block (i, j) from the tread block (i, j). Thus, $\mathbf{F}_{ij} = (F_{xij}, F_{yij})$ is non-zero only when (i, j) is in the tire tread area. The tire body viscoelastic spring parameters (k, γ) and (k', γ') in the tread area and in the side wall area (eight parameters) have been optimized in order to reproduce a number of measured tire properties (e.g. the longitudinal and transverse tire stiffness values for three tire loads, and the frequency and damping of the lowest longitudinal and transverse tire vibrational modes). The optimization has been performed using the amoeba method of multidimensional minimization [21].

4.1. Dependence of the μ-slip curve on the shape of the tire–road footprint

Here we will study how the tire dynamics depend on the shape of the tire–road footprint. We consider the rectangular, elliptic and trapezoid footprints shown in figure 8. We assume first that the pressure in the footprint is uniform and equal to $p = 0.1$ MPa, and that the tire load is equal to 2000 N in all cases. Thus all the footprints have the same area.

In figure 9 we show the μ-slip curves for the three footprints shown in figure 8 and in figure 10 we show the corresponding μ-slip angle curves. It is remarkable how insensitive the results are to the shape of the footprint. Thus we may state that μ-slip curves, and hence tire dynamics, depend very weakly on the shape of the tire–road footprint, assuming everything else is the same.

In figure 11 we show the self-aligning moment for the trapezoid footprint profile in figure 8 as a function of the longitudinal slip (for zero cornering angle). Note that for

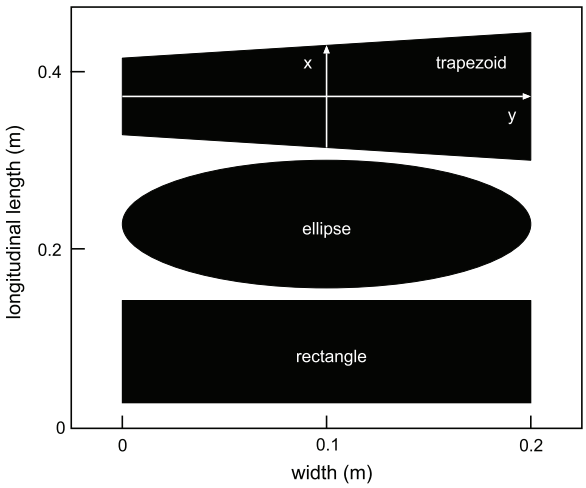

Figure 8. Three tire–road footprints used in the computer simulations. The footprints are 0.2 m wide and the normal pressure in the footprints is constant at $p = 0.1$ or 0.3 MPa.

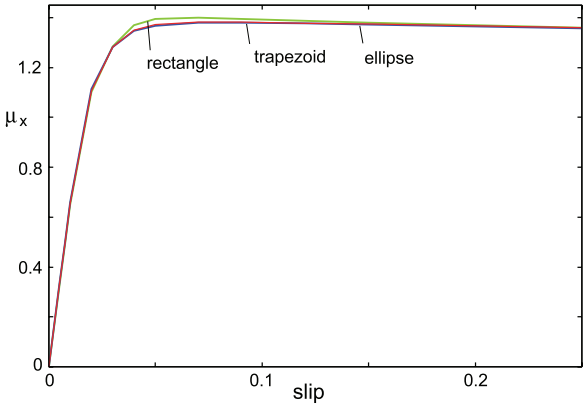

Figure 9. The μ-slip curves for the three footprints shown in figure 8. For the rubber background temperature $T_0 = 80\,^{\circ}$C and the car velocity 27 m s^{-1}. For $F_N = 2000$ N and $p = 0.1$ MPa.

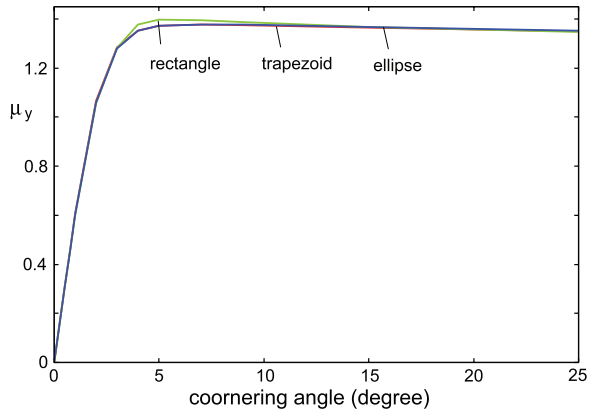

Figure 10. The μ-slip angle curves for the three footprints shown in figure 8. For the rubber background temperature $T_0 = 80\,^{\circ}$C and the car velocity 27 m s^{-1}. For $F_N = 2000$ N and $p = 0.1$ MPa.

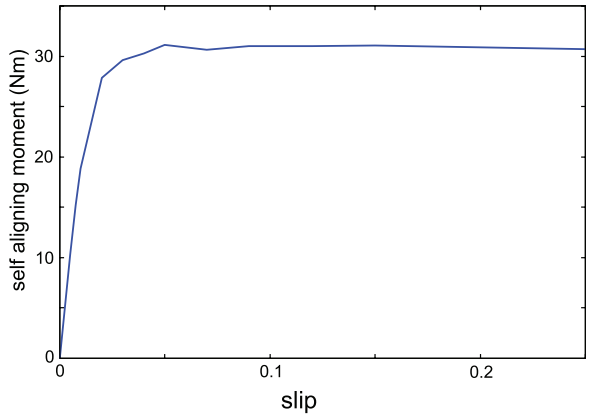

Figure 11. The self-aligning moment for the trapezoid footprint as a function of the longitudinal slip. For the rubber background temperature $T_0 = 80\,^{\circ}$C and the car velocity 27 m s^{-1}. For $F_N = 2000$ N and $p = 0.1$ MPa.

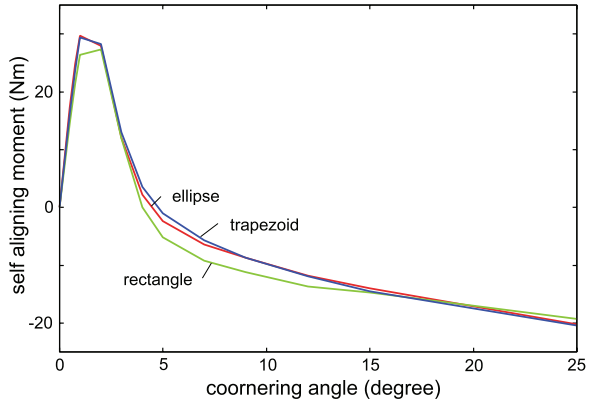

Figure 12. The self-aligning moment for the three footprints shown in figure 8 as a function of the cornering angle. For the rubber background temperature $T_0 = 80\,^{\circ}$C and the car velocity 27 m s^{-1}. For $F_N = 2000$ N and $p = 0.1$ MPa.

the rectangular and elliptic footprint the self-aligning moment vanishes (not shown). This is expected because of the mirror symmetry of the footprint in the x axis through the center of the footprint. However, the trapezoid footprint does not exhibit this symmetry (see figure 8), and the self-aligning moment is non-vanishing in this case.

In figure 12 we show the self-aligning moment for the three footprints shown in figure 8 as a function of the cornering angle (for zero longitudinal slip). In this case the self-aligning moment is non-vanishing in all cases. It is remarkable, however, how insensitive the results are to the shape of the footprint.

For small θ the self-aligning moment is positive. This is due to the gradual (nearly linear) build up of the transverse stress from the inlet of the footprint to the exit. Thus the center of mass of the frictional stress distribution is located closer to the exit of the footprint, giving a positive self-aligning moment. For large θ the self-aligning moment is negative. In the present model this is due to the flash temperature effect: when a tread block enters the footprint the rubber is 'cold' and initially the rubber friction is high. After a short slip distance the full flash temperature is built up and the rubber friction is smaller. This will result in a frictional stress distribution which is larger close

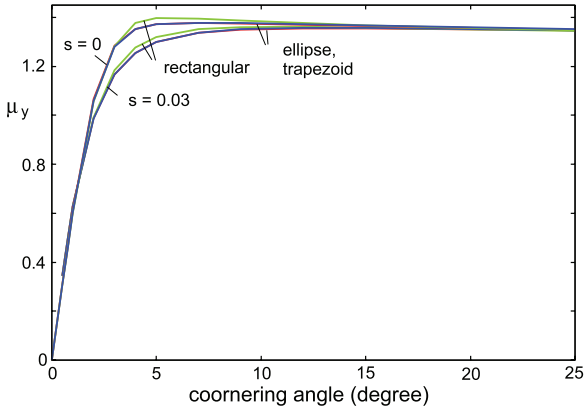

Figure 13. The μ-slip angle curves for the three footprints shown in figure 8 and for the longitudinal slip $s = 0$ and 0.03. For the rubber background temperature $T_0 = 80\,^{\circ}$C and the car velocity 27 m s^{-1}. For $F_N = 2000$ N and $p = 0.1$ MPa.

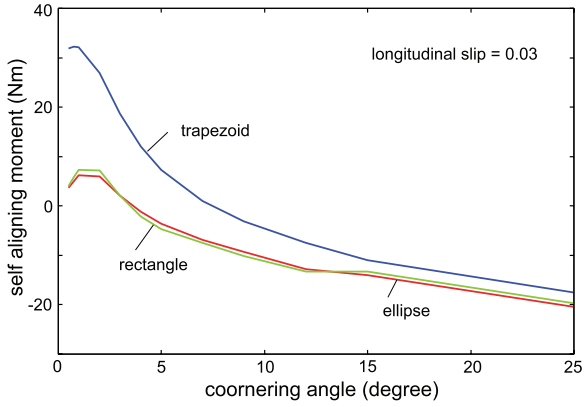

Figure 14. The self-aligning moment for the three footprints shown in figure 8 and for the longitudinal slip $s = 0.03$. For the rubber background temperature $T_0 = 80\,^{\circ}$C and the car velocity 27 m s^{-1}. For $F_N = 2000$ N and $p = 0.1$ MPa.

to the inlet. This in turn results in a negative self-aligning moment.

In the study above we have assumed a constant pressure in the footprints. In reality, the pressure will be slightly larger at the inlet than at the exit of contact with the road (this is the case also during pure rolling and is related to the rolling resistance). This asymmetry will give an additional (negative) contribution to self-aligning moment for large slip.

In figure 13 we show the μ-slip angle curves for the three footprints shown in figure 8, and for the longitudinal slip $s = 0$ and 0.03. Note, in accordance with experimental observations, for the combined slip $\mu_y(\theta)$ is smaller than for the case when the longitudinal slip vanishes. Again there is very little influence on the shape of the footprint. However, the self-aligning moment will now depend strongly on the shape of the footprint. This is shown in figure 14 for the case $s = 0.03$. Note that for the trapezoid footprint the self-aligning moment is much larger than for the elliptic and rectangular footprints. This is due to the contribution from the longitudinal stress component which gives rise to a net longitudinal force centered to the right of the mid-line of the tire.

Figure 15 shows the μ-slip angle curves (a), and the self-aligning moment (b) for the elliptic footprint for the tire load $F_N = 3000$, 5000 and 7000 N, and the footprint pressure $p = 0.3$ MPa. Note that, as the load increases, the footprint becomes longer which results in a decrease in the maximum friction coefficient, which agrees with experimental observations. This load dependence is not due to an intrinsic pressure dependence of the rubber friction coefficient (which was kept constant in our calculation), but a kinetic effect related to the build up of the flash temperature in rubber–road asperity contact regions during slip. To understand this in more detail, consider again figure 1.

The red and blue lines in figure 1 show the kinetic friction coefficient (stationary sliding) as a function of the logarithm of the sliding velocity. The upper line denoted 'cold' is without the flash temperature while the lower line denoted 'hot' is with the flash temperature. The black curves show the effective friction experienced by a tread block as it goes through the

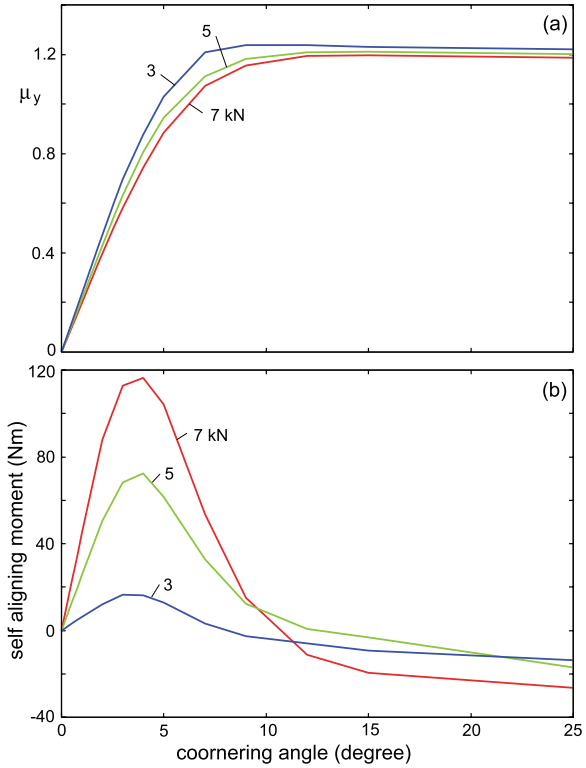

Figure 15. The μ-slip angle curves (a), and the self-aligning moment (b) for the elliptic footprint for the tire load $F_N = 3000$, 5000 and 7000 N, and the footprint pressure $p = 0.3$ MPa. For the rubber background temperature $T_0 = 80\,^{\circ}$C and the car velocity 27 m s^{-1}.

footprint. Results are shown for several slip values 0.005, 0.0075, 0.01, 0.03, 0.05, 0.07 and 0.09. Note that the friction experienced by the tread block first follows the 'cold' rubber branch, and then, when the block has slipped a distance of the order of the diameter D of the macroasperity contact region, it follows the 'hot' rubber branch. Based on this figure it is easy to understand why the maximum friction coefficient increases when the length of the footprint decreases: if v_{slip}

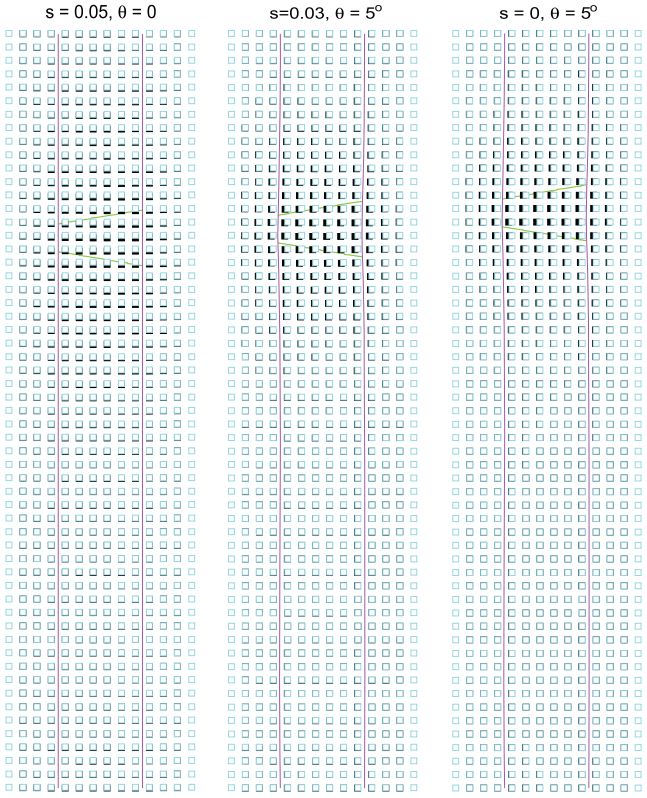

Figure 16. Snapshot pictures of the tire body deformations for slip s and the cornering angle θ given by $(s, \theta) = (0.05, 0°)$ (left), $(0.03, 5°)$ (middle) and $(0, 5°)$ (right). The open squares denote the position of rubber elements of the undeformed tire body and the filled squares underneath denote the position of the same tire body elements of the deformed tire. For the trapezoid contact area with contact pressure 0.1 MPa and normal load $F_N = 2000$ N. For the rubber background temperature $T_0 = 80\,°C$ and the car velocity 27 m s^{-1}.

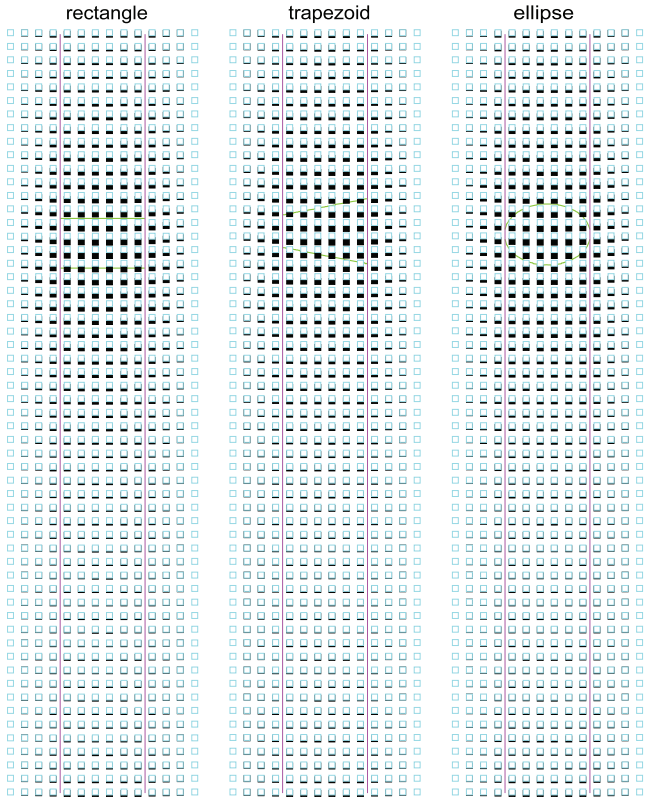

Figure 17. Snapshot pictures of the tire body deformations for the rectangular, trapezoid and elliptic contact area with contact pressure 0.3 MPa and normal load $F_N = 7000$ N. For the slip $s = 0.05$ and the cornering angle $\theta = 0$. For the rubber background temperature $T_0 = 80\,°C$ and the car velocity 27 m s^{-1}.

is the (average) slip velocity of the tread block, then in order to fully build up the flash temperature the following condition must be satisfied: $v_{slip} t_{slip} \approx D$, where D is the diameter of the macroasperity contact region. Since the time the rubber block stays in the footprint $t_{slip} = L/v_R$ (where L is the length of the footprint and v_R the rolling velocity) we get $v_{slip} \approx v_R(D/L)$. Thus, when the length L of the footprint decreases, the (average) slip velocity of the tread block in the footprint can increase without the slip distance exceeding the diameter D of the macroasperity contact region. As a consequence, as L decreases, the tread block will follow the 'cold' rubber branch of the (steady state) μ-slip curve to higher slip velocities before the flash temperature is fully developed, resulting in a higher (maximal) tire–road friction for a short footprint as compared to a longer footprint.

In figure 16 we show snapshot pictures of the tire body deformations for three cases, namely with the slip s and the cornering angle θ given by $(s, \theta) = (0.05, 0°)$ (left), $(0.03, 5°)$ (middle) and $(0, 5°)$ (right). The open squares denote the position of rubber elements of the undeformed tire body and the filled squares underneath denote the position of the same tire body elements of the deformed tire.

In figure 17 we show snapshot pictures of the tire body deformations for the rectangular, trapezoid and elliptic contact area with contact pressure 0.3 MPa and normal load $F_N = 7000$ N. In all cases the slip $s = 0.05$ and the cornering angle $\theta = 0$. Note how insensitive the deformation field is to the shape of the footprint. This is caused by the high stiffness of the tire body in the tread area.

4.2. Dependence of the μ-slip curve on the size of the tire–road footprint

In figure 18 we show μ-slip curves for the rectangular footprint for the contact pressures $p = 0.1$, 0.125, 0.15 and 0.3 MPa. The tire load is fixed at $F_N = 2000$ so the different contact pressures corresponding to the footprint length $L = 10.2$, 8.1, 6.8 and 3.4 cm, respectively. Note that increasing the tire footprint pressure decreases the length of the footprint, which decreases the tire longitudinal stiffness C_x (determined by the initial slope of the $\mu_x(s)$ curves) and also the maximum of the μ-slip curves. In practice the pressure in the tire–road footprint can be changed by changing the tire inflation pressure, but in this case one expects also a change in the tire body stiffness. In the tire model we use, this effect is not included at present. Thus, at least for passenger car tires, when the inflation pressure increases the longitudinal tire stiffness C_x usually first increases and then, at high enough inflation pressure, decreases. This is consistent with figure 18 which shows initially a very small change in the tire stiffness as the

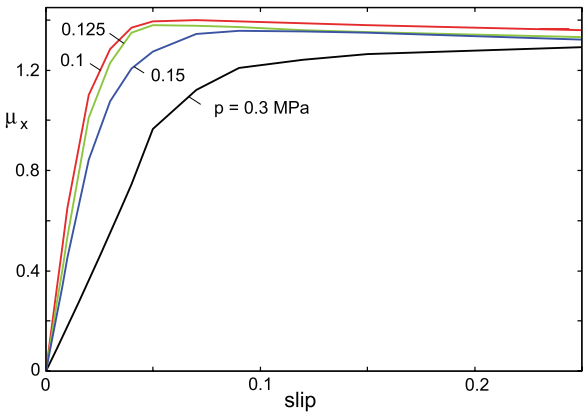

Figure 18. The μ-slip curves for the rectangular footprint shown in figure 8. For the contact pressures $p = 0.1$, 0.125, 0.15 and 0.3 MPa corresponding to the footprint length $L = 10.2$, 8.1, 6.8 and 3.4 cm. For the rubber background temperature $T_0 = 80\,^{\circ}\mathrm{C}$, the tire load $F_N = 2000$ and the car velocity 27 m s^{-1}.

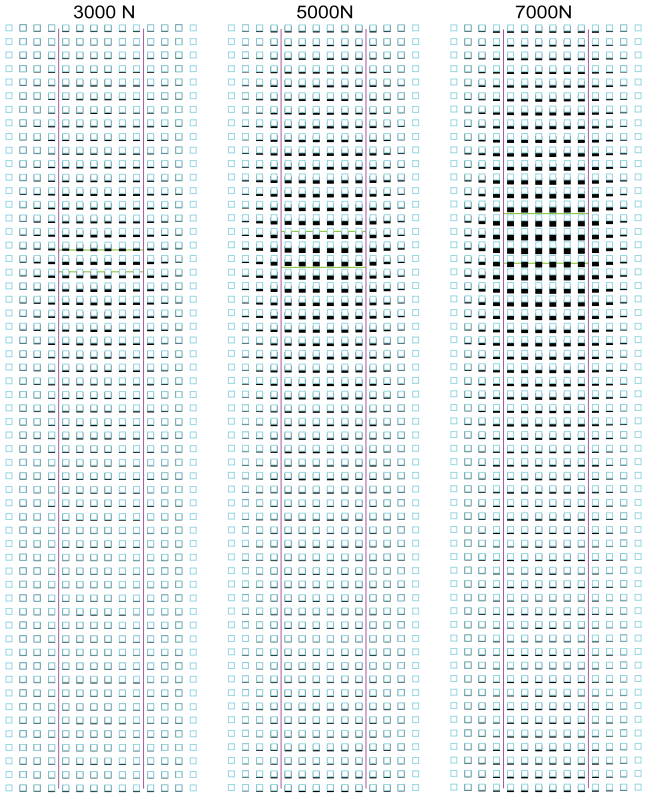

Figure 19. Snapshot pictures of the tire body deformations for the normal load $F_N = 3000$, 5000 and 7000 N. In all cases the slip $s = 0.05$ and the cornering angle $\theta = 0$. The maximum tire body displacements are 0.92, 1.39 and 1.84 cm for the tire loads $F_N = 3000$, 5000 and 7000 N, respectively. For the rectangular contact area with contact pressure 0.3 MPa. For the rubber background temperature $T_0 = 80\,^{\circ}\mathrm{C}$ and the car velocity 27 m s^{-1}.

footprint pressure p increases, so that for small (but not too small) p the stiffening of the tire body may dominate over the contribution from the change in the footprint, so that initially C_x increases with increasing p.

In figure 19 we show snapshot pictures of the tire body deformations for three cases, namely for the external load

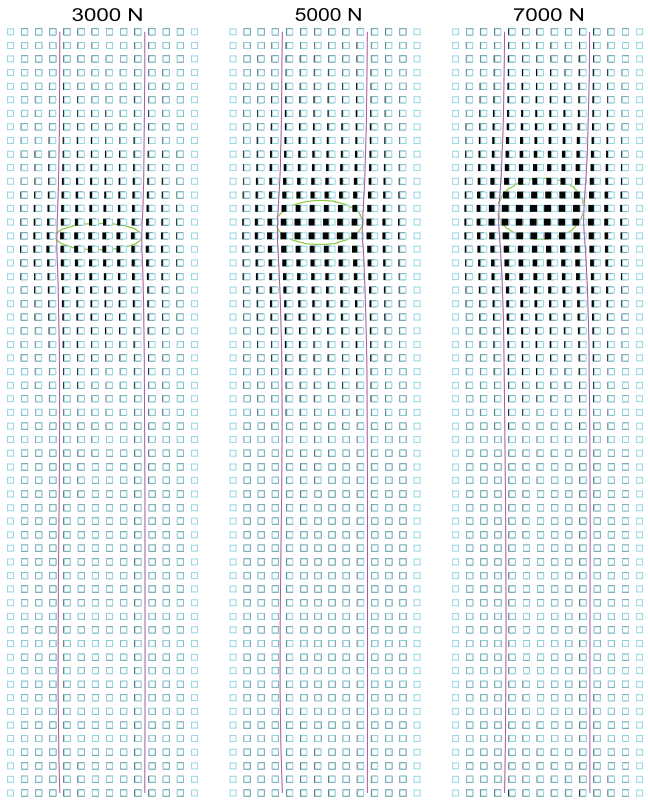

Figure 20. Snapshot pictures of the tire body deformations for the normal load $F_N = 3000$, 5000 and 7000 N. In all cases the slip $s = 0$ and the cornering angle $\theta = 5°$. The maximum tire body displacements are 1.20, 1.81 and 2.31 cm for the tire loads $F_N = 3000$, 5000 and 7000 N, respectively. For the elliptic contact area with contact pressure 0.3 MPa. For the rubber background temperature $T_0 = 80\,^{\circ}\mathrm{C}$ and the car velocity 27 m s^{-1}.

$F_N = 3000$, 5000 and 7000 N. In all cases the slip $s = 0.05$ and the cornering angle $\theta = 0$. The results are for the rectangular footprint with contact pressure 0.3 MPa.

In figure 20 we show similar results as in figure 19 but now for the elliptic contact area with contact pressure 0.3 MPa, and with the slip $s = 0$ and the cornering angle $\theta = 5°$. The maximum tire body displacements are 1.20, 1.81 and 2.31 cm for the tire loads $F_N = 3000$, 5000 and 7000 N, respectively.

In figure 21 we show the maximum friction coefficient, μ_{max}, of the μ_x-slip curve for the elliptic, rectangular and trapezoid footprints, as a function of the tire load. We show results for the contact pressures $p = 0.1$ MPa (upper three curves) and 0.3 MPa (lower three curves), but the tire body properties are assumed to be the same. Note that the effective friction depends on the (average) tire–road footprint pressure p. When p increases, assuming an unchanged size of the footprint, the friction decreases. This is one reason for why race tires exhibit much larger friction than passenger car tires (the contact pressure in F1 tires is of the order of 0.1 MPa, which is about three times lower than in passenger car tires). The increase in the friction as the tire–road contact pressure p decreases is mainly due to a decrease in the pressure in the macroasperity contact regions as p decreases: when the local pressure decreases the produced heating of the rubber decreases leading to a larger friction.

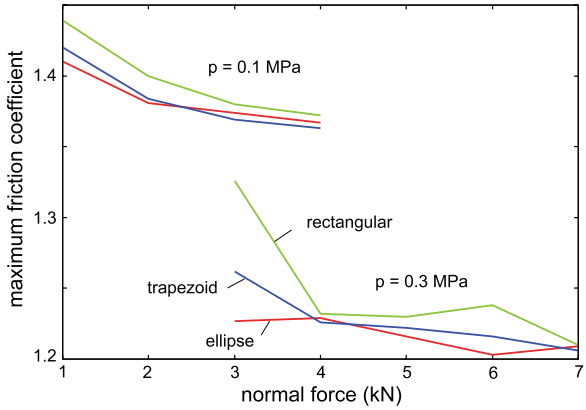

Figure 21. The maximum friction coefficient, $\mu_{\max}$, of the μ_x-slip curve for elliptic, rectangular and trapezoid footprints. For the contact pressures $p = 0.1$ MPa (upper three curves) and 0.3 MPa (lower three curves). For the rubber background temperature $T_0 = 80\,^{\circ}$C and the car velocity 27 m s^{-1}.

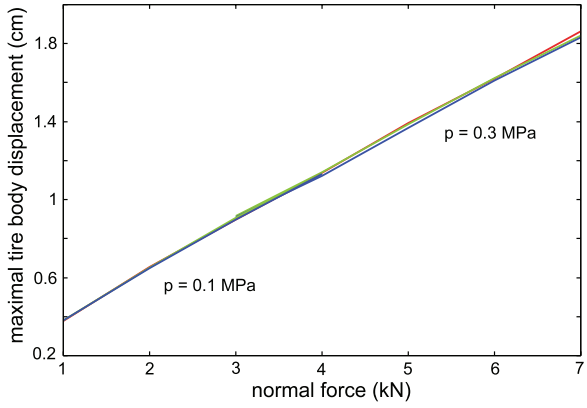

Figure 23. The maximum longitudinal tire body displacement for elliptic, rectangular and trapezoid footprints. For the contact pressures $p = 0.1$ MPa (lower three curves) and 0.3 MPa (upper three curves). For the rubber background temperature $T_0 = 80\,^{\circ}$C and the car velocity 27 m s^{-1}.

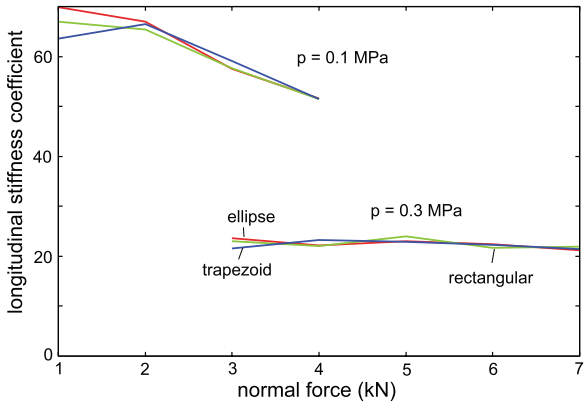

Figure 22. The longitudinal tire stiffness $C_{\rm L}$ associated with the μ_x-slip curve for elliptic, rectangular and trapezoid footprints. For the contact pressures $p = 0.1$ MPa (upper three curves) and 0.3 MPa (lower three curves). For the rubber background temperature $T_0 = 80\,^{\circ}$C and the car velocity 27 m s^{-1}.

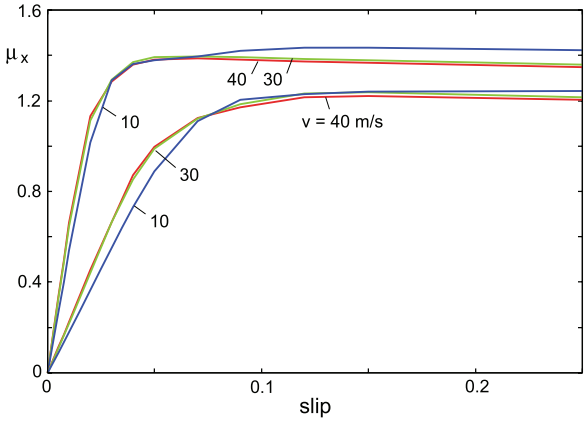

Figure 24. The μ-slip curves for a rectangular footprint (20 cm $\times$ 10.2 cm) and for the car velocities $v_{\rm c} = 10$, 30 and 40 m s^{-1}. For $F_{\rm N} = 2000$ N and $p = 0.1$ MPa (top three curves) and $F_{\rm N} = 6000$ N and $p = 0.3$ MPa (lower three curves). For the rubber background temperature $T_0 = 80\,^{\circ}$C.

In figure 22 we show for the same systems the longitudinal tire stiffness C_x associated with the μ_x-slip curves. Finally, figure 23 gives the maximum longitudinal tire body displacement as a function of the tire load for the same systems as in figure 21.

4.3. Dependence of the μ-slip curve on the car velocity

Figure 24 shows the μ-slip curves for the rectangular footprint (20 cm $\times$ 10.2 cm) shown in figure 8, and for the car velocities $v_{\rm c} = 10$, 30 and 40 m s^{-1}. We show results both for the tire load $F_{\rm N} = 2000$ N and $p = 0.1$ MPa (top three curves) and for $F_{\rm N} = 6000$ N and $p = 0.3$ MPa (lower three curves). Note that, as the car velocity decreases, the longitudinal tire stiffness C_x decreases and the maximum of the μ-slip curve increases. This is in accordance with experimental observations for passenger car tires (see, e.g., figure 8.65 in [3]). When the contact pressure and the load both increase, in such a way that the contact area stays constant, both the tire stiffness and the maximum of the μ-slip curves decrease.

5. ABS braking simulations

The theory developed above may be extremely useful to design or optimize control algorithms for ABS braking. Here we will present results using the two simplest possible control algorithms. In both cases the braking torque is changed (increased or decreased) in steps of ΔM at time $t_n = n\Delta t\,(n = 1, 2, \ldots)$. The first algorithm (a) assumes that the slip s^* where the friction is maximal is known (and constant in time). In this case the braking torque is increased if the slip $s(t_n)$ at time t_n is below s^* and otherwise it is decreased, see figure 25. One problem here is that the slip s^* depends on the car velocity which changes during the braking process. However, in the present case $s^* \approx 0.057$ nearly independent of the car velocity for 10 m s^{-1} $< v_{\rm c} <$ 27 m s^{-1}. Note that s^* will also depend on the increase in the background temperature T_0 due to the

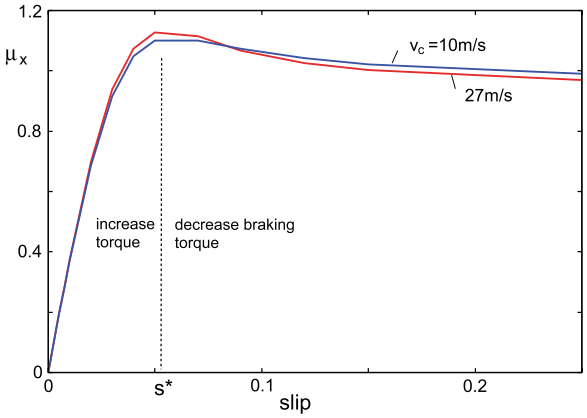

Figure 25. The μ-slip curves for the car velocity $v_c = 10$ and 27 m s^{-1}. The maximum μ^* of the μ-slip curve, and the slip $s = s^*$ where the maximum occurs, depends on the car velocity v_c. In the present case $s^* \approx 0.057$ for both velocities. The ABS control algorithm should increase the braking torque when $s < s^*$ and reduce the braking torque when $s > s^*$.

frictional heating of the tire during the braking, but this effect is not included in the present study.

In the second control algorithm (b) we assume that s^* is unknown. Nevertheless, by registering if the (longitudinal) friction $F_x(t)$ is increasing or decreasing with time we can find out if we are to the left or right of the maximum at $s = s^*$. That is, if

$$F_x(t_n) > F_x(t_{n-1}) \qquad \text{and} \qquad s(t_n) < s(t_{n-1})$$

or if

$$F_x(t_n) < F_x(t_{n-1}) \qquad \text{and} \qquad s(t_n) > s(t_{n-1})$$

then we must have $s(t_n) > s^*$ and the braking torque at time t_n is reduced, otherwise it is increased. Here $F_x(t_n)$ is the longitudinal friction force and $s(t_n)$ the slip at time $t_n = n\Delta t (n = 1, 2, \ldots)$.

We now present numerical results to illustrate the two ABS braking algorithms. Let M be the mass-load on a wheel and I the moment of inertia of the wheel without the tire. We assume for simplicity that the suspension is rigid and neglect mass-load transfer. The equations of motion for the center-of-mass coordinate $x(t)$ of the wheel and for the angular rotation coordinate $\phi(t)$ are

$$M\ddot{x} = F_{\text{rim}} \tag{2}$$

$$I\ddot{\phi} = M_{\text{rim}} - M_{\text{B}} \tag{3}$$

where F_{rim} is the force acting on the rim, M_{B} is the braking torque and M_{rim} the torque acting on the rim from the tire (for constant rolling velocity $F_{\text{rim}} = F_{\text{f}}$ is the tire–road friction force and $M_{\text{rim}} = RF_{\text{f}}$, where R is the rolling radius, but during angular accelerations these relations no longer hold because of tire inertia effects). We have used $M = 360$ kg and $I = 0.4$ kg m^2.

We assume first the control algorithm (a). We take $\Delta M = 200$ N m and $\Delta t = 0.03$ s, and we assume (see figure 25) $s^* \approx 0.05$. In figure 26 we show (a) the car velocity v_c and the rolling velocity v_R, (b) the longitudinal slip and (c) the braking torque as a function of time. The time it takes ($t = 1.775$ s) to reduce the car velocity from $v_0 = 27$ to $v_1 = 10$ m s^{-1} corresponds to a friction coefficient $\mu = (v_0 - v_1)/gt = 0.976$, which is ∼13% smaller than the friction at the maximum of the μ-slip curve, which varies between $\mu_{\text{max}} = 1.14$ and 1.11 as the car velocity changes from 27 to 10 m s^{-1}. The slope of the car-velocity line in figure 26(a) for $t > 0.2$ s corresponds to the friction coefficient 1.02, which is larger than the (average) friction calculated from the stopping time. The slightly smaller friction obtained from the stopping time reflects the (short) initial time interval necessary to build up the braking torque.

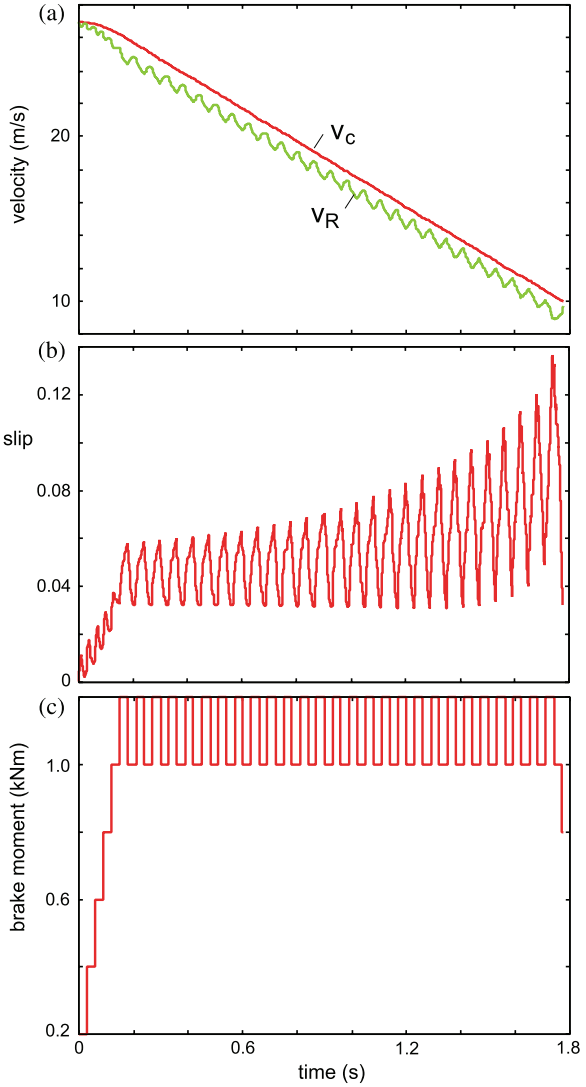

Figure 26. (a) The car velocity v_c and the rolling velocity v_R as a function of time t. (b) The slip and (c) the braking moment as a function of time t. For ABS braking using algorithm **a** (see text for details).

In figure 27 we show results for the ABS control algorithm (b). Note that it takes $t = 1.949$ s to reduce the car velocity from $v_0 = 27$ m s^{-1} to $v_1 = 10$ m s^{-1}. This corresponds to the effective friction coefficient $\mu = (v_0 - v_1)/gt = 0.889$, which is slightly smaller than the effective friction obtained using ABS control algorithm (a).

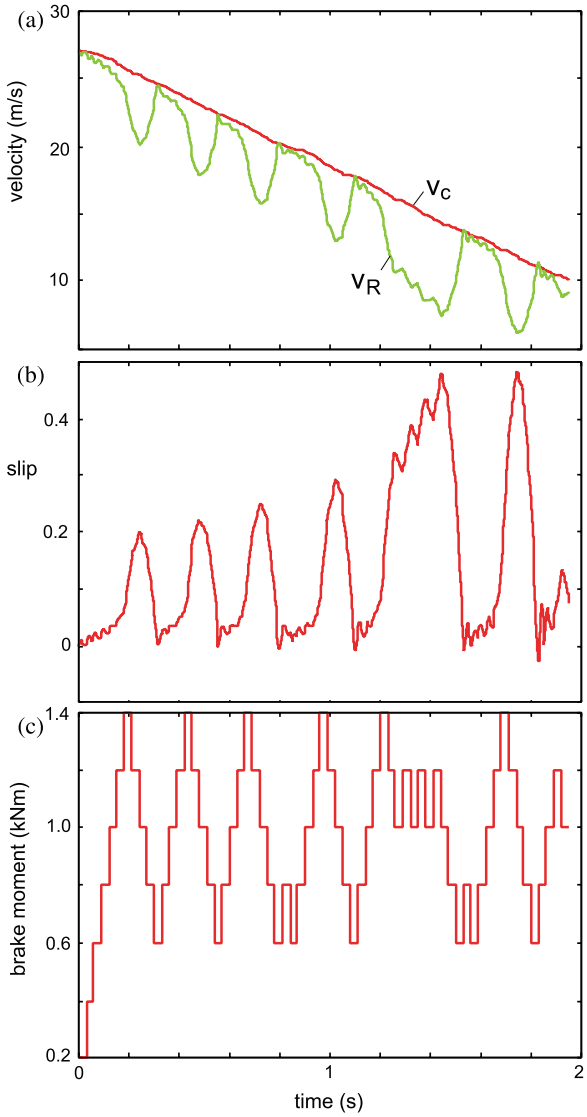

Figure 27. (a) The car velocity v_c and the rolling velocity v_R as a function of time t. (b) The slip and (c) the braking moment as a function of time t. For ABS braking using algorithm **b** (see text for details).

The maximum in the μ-slip curve (see figure 25) depends on the car velocity but is about $\mu_{max} = 1.14$ for $v_c = 27$ m s^{-1} and about 1.11 for $v_c = 10$ m s^{-1} so the ABS braking control algorithm used above could still be improved. Note also that the wheel tends to lock about 3 or 4 times per second. This is in good agreement with ABS braking systems presently in use. However, since the speed of cars is usually not known during ABS braking, braking control algorithms used in most cars today determine the braking torque only from the wheel rotation acceleration. This is possible because, as shown in figure 27(a), as the wheel tends to lock, the rotational velocity very rapidly decreases, and at this point the ABS system decreases the braking torque.

Note that the (average) of the slip in figures 26(b) and 27(b) increases with increasing time or, equivalently, decreasing car velocity. This is due to the fact that the time it takes for the wheel to lock, when the slip $s > s^*$, decreases as v_c decreases. Thus, during the time period Δt between two changes in the brake torque the maximal slip (corresponding to the minimal rolling velocity) will increase as v_c decreases. This is easy to show mathematically. Since the car velocity changes slowly compared to the rolling velocity, from the definition $s = (v_c - v_R)/v_c$ we get

$$\frac{dv_R}{dt} \approx -v_c \frac{ds}{dt}.$$

If we approximate the μ-slip curve for $s > s^*$ with a straight line

$$\mu_{eff} \approx \mu_0 - \Delta\mu s,$$

we get from (3)

$$I\frac{d^2\phi}{dt^2} = \frac{I}{R}\frac{dv_R}{dt} \approx -\frac{Iv_c}{R}\frac{ds}{dt} = MgR[\mu_0 - \Delta\mu s] - M_B$$

or

$$\frac{ds}{dt} = -A + Bs$$

where $A = (MgR\mu_0 - M_B)(R/Iv_c)$ and $B = \Delta\mu\,(MgR^2/Iv_c)$. Since A and B can be considered as constant during the time interval between the changes in the braking torque, we get

$$s(t) = \left(s(0) - \frac{A}{B}\right)e^{Bt} + \frac{A}{B}$$

where

$$\frac{A}{B} = \frac{1}{\Delta\mu}\left(\mu_0 - \frac{M_B}{MgR}\right).$$

It is easy to show that

$$s(0) - \frac{A}{B} = [s(0) - s^*] + \frac{M_B - M_B^*}{\Delta\mu MgR}$$

where $M_B^* = Mg(\mu_0 - \Delta\mu s^*)$ is the braking torque necessary in order to stay at the maximum in the μ-slip curve. If $s(0) > s^*$ and the braking torque $M_B > M_B^* - \Delta\mu MgR[s(0) - s^*]$ we have $s(0) - A/B > 0$ and during the time interval Δt the slip will increase with $[s(0) - A/B]\exp(B\Delta t)$. Since $B\Delta t \sim 1/v_c$ the maximum slip will increase exponentially (until the wheel block, corresponding to $s = 1$) with the inverse of the car velocity. This behavior (i.e. the increase in the slip with decreasing car velocity) can be seen in figure 26(b) and is even stronger for the second ABS control algorithm (figure 27(b)).

In figure 28 we show the μ-slip curve during stationary slip (green curve) and the instantaneous effective friction coefficient $\mu_{eff}(t) = F_x(t)/F_N$ during braking (blue curve).

The blue and red curves in figure 29 show the car velocity using the ABS control algorithms (a) and (b). It is clear that the ABS control algorithm (a) is more effective than algorithm (b), but algorithm (a) assumes that s^* is known and remains constant during the braking event.

The ABS braking control algorithms used today usually assume that only the wheel rolling velocity $v_R(t)$ is known. Basically, whenever a wheel tends to lock-up, which manifests itself in a large (negative) wheel angular acceleration, the

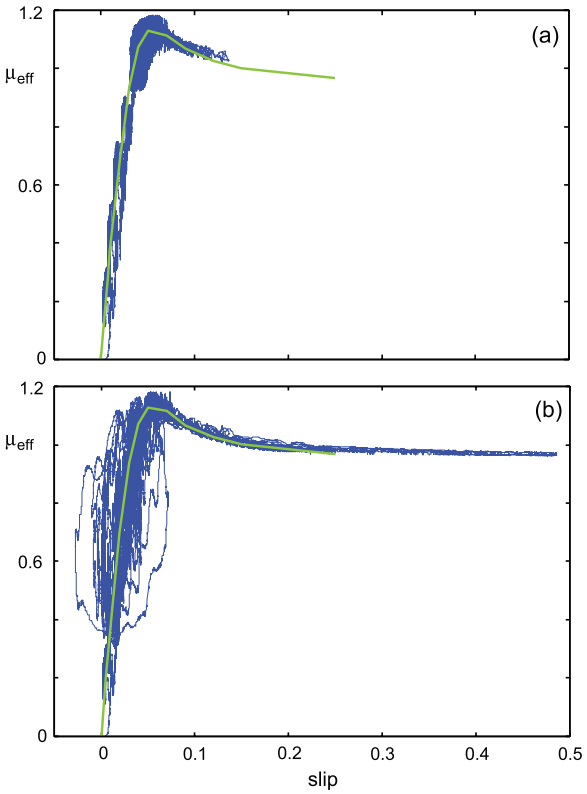

Figure 28. Dynamical μ-slip curves for ABS braking using algorithms **a** (top) and **b** (bottom). The green curve is the steady state μ-slip curve for the car velocity $v_c = 27$ m s^{-1}.

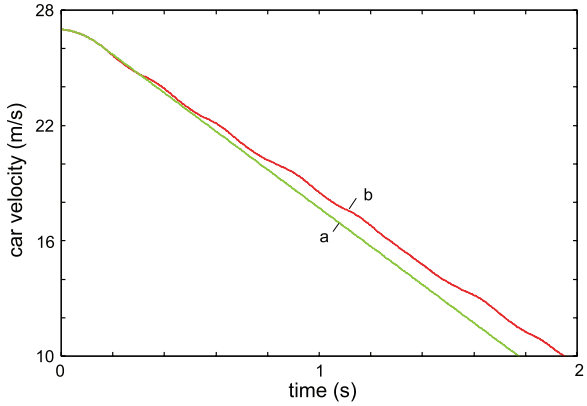

Figure 29. The car velocity v_c as a function of time t during ABS braking using two algorithms **a** and **b**. The procedures **a** and **b** results in the time periods 1.76 and 1.95 s for reducing the car velocity from 27 to 10 m s^{-1}. The effective friction values 0.976 and 0.889 are both smaller than the maximum kinetic friction which is 1.098 and occurs at the slip velocity 0.0316 m s^{-1}.

braking torque is reduced. These ABS braking control algorithms (e.g. the Bosch algorithm) are rather complex and secret. The calculations presented above can be easily extended to such realistic ABS braking control algorithms and to more complex cases such as braking during load fluctuations (e.g. braking on uneven road surfaces) and switching between different road surfaces (by using different road surface power spectra during an ABS braking simulation).

6. Summary and conclusion

In this paper we have proposed a simple rubber friction law, which can be used, for example, in models of tire (and vehicle) dynamics. The friction law gives nearly the same result as the full rubber friction theory of [6], but is much more convenient to use in numerical studies of, for example, tire dynamics, as the friction force can be calculated much faster.

We have proposed a two-dimensional (2D) tire model which combines the rubber friction law with a simple mass–spring description of the tire body. The tire model is very flexible and can be used to calculate accurate μ-slip (and self-aligning torque) curves for braking and cornering or combined motion (e.g. braking during cornering). We have presented numerical results which illustrate the theory. Simulations of anti-blocking system (ABS) braking was performed using two simple control algorithms.

References

[1] Persson B N J 2000 *Sliding Friction: Physical Principles and Applications* 2nd edn (Heidelberg: Springer)
[2] Grosch K A 1963 *Proc. R. Soc.* A **274** 21
[3] Gent A N and Walter J D (ed) 2006 *The Pneumatic Tire* US Department of Transportation (Washington, DC: NHTSA)
[4] Pacejka H B 2006 *Tyre and Vehicle Dynamics* 2nd edn (Amsterdam: Elsevier)
[5] Persson B N J 2001 *J. Chem. Phys.* **115** 3840
[6] Persson B N J 2006 *J. Phys.: Condens. Matter* **18** 7789
[7] Heinrich G, Klüppel M and Vilgis T A 2000 *Comput. Theor. Polym. Sci.* **10** 53
[8] Heinrich G and Klüppel M 2008 *Wear* **265** 1052
[9] Klüppel M and Heinrich G 2000 *Rubber Chem. Technol.* **73** 578
[10] Westermann S, Petry F, Boes R and Thielen G 2004 *Kautsch. Gummi Kunstst.* **57** 645
[11] Persson B N J and Volokitin A I 2006 *Eur. Phys. J.* E **21** 69
[12] Carbone G, Lorenz B, Persson B N J and Wohlers A 2009 *Eur. Phys. J.* E **29** 275
[13] Persson B N J 1998 *Surf. Sci.* **401** 445
[14] Le Gal A and Klüppel M 2005 *J. Chem. Phys.* **123** 014704
[15] Persson B N J 2009 *J. Phys.: Condens. Matter* **21** 485001
[16] Mofidi M, Prakash B, Persson B N J and Albohr O 2008 *J. Phys.: Condens. Matter* **20** 085223
[17] See, e.g. Persson B N J, Albohr O, Tartaglino U, Volokitin A I and Tosatti E 2005 *J. Phys.: Condens. Matter* **17** R1
[18] Persson B N J, Albohr O, Creton C and Peveri V 2004 *J. Chem. Phys.* **120** 8779
[19] Lorenz B and Persson B N J 2010 unpublished
[20] Persson B N J 2006 *Surf. Sci. Rep.* **61** 201
[21] See, e.g., sec. 10.4 in Press W H, Teukolsky S A, Vetterling W T and Flannery B P (ed) 1992 *Numerical Recipes* 2nd edn (Cambridge: Cambridge University Press)